

Probing the Electronic Structure of Complex Systems by ARPES

To cite this article: Andrea Damascelli 2004 *Phys. Scr.* **2004** 61

View the [article online](#) for updates and enhancements.

You may also like

- [Electronic properties of candidate type-II Weyl semimetal \$\text{WTe}_2\$: A review perspective](#)
P K Das, D Di Sante, F Cilento et al.
- [Angle-resolved photoemission spectroscopy studies of metallic surface and interface states of oxide insulators](#)
Nicholas C Plumb and Milan Radovi
- [Relaxation of strongly coupled electron and phonon fields after photoemission and high-energy part of ARPES spectra of cuprates](#)
A E Myasnikova, E A Zhileeva and D V Moseykin

Recent citations

- [Anomalous Hall transport in tilted multi-Weyl semimetals](#)
Anirudha Menon and Banasri Basu
- [K-means-driven Gaussian Process data collection for angle-resolved photoemission spectroscopy](#)
Charles N Melton *et al*
- [Production and processing of graphene and related materials](#)
Claudia Backes *et al*

Probing the Electronic Structure of Complex Systems by ARPES

Andrea Damascelli

Department of Physics & Astronomy, University of British Columbia, 6224 Agricultural Road, Vancouver, British Columbia V6T 1Z1, Canada

Received June 18, 2003; accepted June 30, 2003

PACS Ref: 79.60.i, 71.18.+y; 71.20.-b

Abstract

Angle-resolved photoemission spectroscopy (ARPES) is one of the most direct methods of studying the electronic structure of solids. By measuring the kinetic energy and angular distribution of the electrons photoemitted from a sample illuminated with sufficiently high-energy radiation, one can gain information on both the energy and momentum of the electrons propagating inside a material. This is of vital importance in elucidating the connection between electronic, magnetic, and chemical structure of solids, in particular for those complex systems which cannot be appropriately described within the independent-particle picture. The last decade witnessed significant progress in this technique and its applications, thus ushering in a new era in photoelectron spectroscopy; today, ARPES experiments with 2 meV energy resolution and 0.2° angular resolution are a reality even for photoemission on solids. In this paper we will review the fundamentals of the technique and present some illustrative experimental results; we will show how ARPES can probe the momentum-dependent electronic structure of solids providing detailed information on band dispersion and Fermi surface as well as on the strength and nature of many-body correlations, which may profoundly affect the one-electron excitation spectrum and in turn the macroscopic physical properties.

1. Introduction

Photoelectron spectroscopy is a general term that refers to all those techniques based on the application of the photoelectric effect originally observed by Hertz [1] and later explained as a manifestation of the quantum nature of light by Einstein [2], who recognized that when light is incident on a sample an electron can absorb a photon and escape from the material with a maximum kinetic energy $E_{kin} = h\nu - \phi$ (where ν is the photon frequency and ϕ , the material work function, is a measure of the potential barrier at the surface that prevents the valence electrons from escaping, and is typically 4–5 eV in metals). In the following, we will show how the photoelectric effect also provides us with deep insights into the quantum description of the solid state. In particular, we will give a general overview of angle-resolved photoemission spectroscopy (so-called ARPES), a highly advanced spectroscopic method that allows the direct experimental study of the momentum-dependent electronic band structure of solids. For a further discussion of ARPES and other spectroscopic techniques based on the detection of photoemitted electrons, we refer the reader to the extensive literature available on the subject [3–34].

As we will see in detail throughout the paper and in particular in Section 3, due to the complexity of the photoemission process in solids the quantitative analysis of the experimental data is often performed under the assumption of the *independent-particle picture* and of the *sudden approximation* (i.e., disregarding the many-body interactions as well as the relaxation of the system during the photoemission itself). The problem is further simplified within the so-called *three-step model* (Fig. 1(a)), in which the

photoemission event is decomposed in three independent steps: optical excitation between the initial and final *bulk* Bloch eigenstates, *travel* of the excited electron to the surface, and escape of the photoelectron into vacuum after transmission through the *surface* potential barrier. This is the most common approach, in particular when photoemission spectroscopy is used as a tool to map the electronic band structure of solids. However, from the quantum-mechanical point of view photoemission should not be described in terms of several independent events but rather as a *one-step* process (Fig. 1(b)): in terms of an optical transition (with probability given by Eq. (12)) between initial and final states consisting of many-body wave functions that obey appropriate boundary conditions at the surface of the solid. In particular (see Fig. 2), the initial state should be one of the possible N -electron eigenstates of the semi-infinite crystal, and the final state must be one of the eigenstates of the ionized $(N - 1)$ -electron semi-infinite crystal; the latter has also to include a component consisting of a propagating plane-wave in vacuum (to account for the escaping photoelectron) with a finite amplitude inside the crystal (to provide some overlap with the initial state). Furthermore, as expressed by Eq. (12) which does represent a complete one-step description of the problem, in order for an electron to be photoemitted in vacuum not only there must be a finite overlap between the amplitude of initial and final states, but also the following energy and momentum conservation laws for the impinging photon and the N -electron system as a whole must be obeyed:

$$E_f^N - E_i^N = h\nu, \quad (1)$$

$$\mathbf{k}_f^N - \mathbf{k}_i^N = \mathbf{k}_{h\nu} \quad (2)$$

where the indexes i and f refer to initial and final state, respectively, and $\mathbf{k}_{h\nu}$ is the momentum of the incoming photon. Note that, in the following, in proceeding with the more detailed analysis of the photoemission process as well as its application to the study of the momentum-dependent electronic structure of solids (in terms of both conventional band mapping as well as many-body effects), we will mainly restrict ourselves to the context of the three-step model and the sudden approximation.

2. Kinematics of photoemission

The energetics and kinematics of the photoemission process are shown in Fig. 3 and 4, while the geometry of an ARPES experiment is sketched in Fig. 6(a). A beam of monochromatized radiation supplied either by a gas-discharge lamp or by a synchrotron beamline is incident on a sample (which has to be a properly aligned single

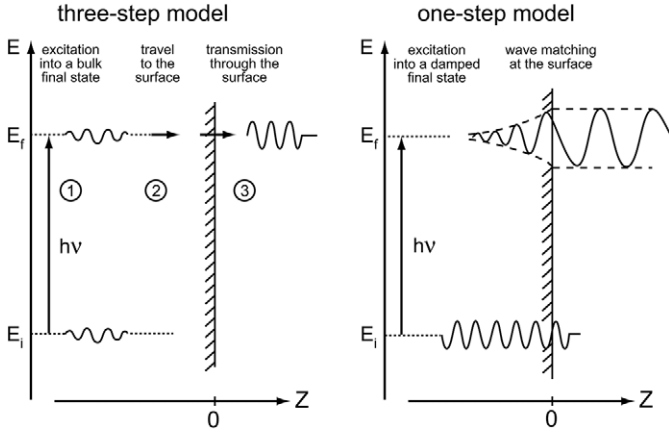


Fig. 1. Pictorial representation of three-step and one-step model descriptions of the photoemission process (from Ref. [17]).

crystal in order to perform *angle* or, equivalently, *momentum*-resolved measurements). As a result, electrons are emitted by photoelectric effect and escape in vacuum in all directions. By collecting the photoelectrons with an electron energy analyzer characterized by a finite acceptance angle, one measures their kinetic energy E_{kin} for a given emission direction. This way, the wave vector or momentum $\mathbf{K} = \mathbf{p}/\hbar$ of the photoelectrons *in vacuum* is also completely determined: its modulus is given by $K = \sqrt{2mE_{kin}}/\hbar$ and its components parallel ($K_{\parallel} = K_x + K_y$) and perpendicular ($K_{\perp} = K_z$) to the sample surface are obtained in terms of the polar (ϑ) and azimuthal (φ) emission angles defined by the experiment:

$$K_x = \frac{1}{\hbar} \sqrt{2mE_{kin}} \sin \vartheta \cos \varphi, \quad (3)$$

$$K_y = \frac{1}{\hbar} \sqrt{2mE_{kin}} \sin \vartheta \sin \varphi, \quad (4)$$

$$K_z = \frac{1}{\hbar} \sqrt{2mE_{kin}} \cos \vartheta. \quad (5)$$

The goal is then to deduce the electronic dispersion relations $E(\mathbf{k})$ for the solid left behind, i.e. the relation between binding energy E_B and momentum \mathbf{k} for the electrons propagating *inside* the solid, starting from E_{kin} and \mathbf{K} measured for the photoelectrons *in vacuum*. In order to do that, one has to exploit the total energy and momentum conservation laws (Eq. (1) and (2), respectively).

Within the non-interacting electron picture, it is particularly straightforward to take advantage of the energy conservation law and relate, as pictorially described in Fig. 3, the kinetic energy of the photoelectron to the binding energy E_B of the electronic-state inside the solid:

$$E_{kin} = h\nu - \phi - |E_B|. \quad (6)$$

More complex, as we will discuss below, is to gain full knowledge of the crystal electronic momentum \mathbf{k} . Note, however, that the photon momentum can be neglected in Eq. (2) at the low photon energies most often used in ARPES experiments ($h\nu < 100$ eV), as it is much smaller than the typical Brillouin-zone dimension $2\pi/a$ of a solid (see Section 6 for more details). Thus, as shown in Fig. 4 within the three-step model description (see also Section 3), the optical transition between the bulk initial and final

states can be described by a vertical transition in the *reduced-zone scheme* ($\mathbf{k}_f - \mathbf{k}_i = 0$), or equivalently by a transition between momentum-space points connected by a reciprocal-lattice vector \mathbf{G} in the *extended-zone scheme* ($\mathbf{k}_f - \mathbf{k}_i = \mathbf{G}$). In regard to Eq. (1) and (2) and the deeper meaning of the reciprocal-lattice vector \mathbf{G} note that, as emphasized by Mahan in his seminal paper on the theory of photoemission in simple metals [36], “*in a nearly-free-electron gas, optical absorption may be viewed as a two-step process. The absorption of the photon provides the electron with the additional energy it needs to get to the excited state. The crystal potential imparts to the electron the additional momentum it needs to reach the excited state. This momentum comes in multiples of the reciprocal-lattice vectors \mathbf{G} . So in a reduced zone picture, the transitions are vertical in wave-vector space. But in photoemission, it is more useful to think in an extended-zone scheme.*”

On the contrary in an infinite crystal with no periodic potential (i.e., a truly free-electron gas scenario lacking of any periodic momentum structure), no \mathbf{k} -conserving transition is possible in the limit $\mathbf{k}_{hv} = 0$, as one cannot go from an initial to a final state along the same unperturbed free-electron parabola without an external source of momentum. In other words, direct transitions are prevented because of the lack of appropriate final states (as opposed to the periodic case of Fig. 4). Then again the problem would be quite different if the surface was more realistically taken into account, as in a one-step model description of a semi-infinite crystal. In fact, while the surface does not perturb the translational symmetry in the x - y plane and \mathbf{k}_{\parallel} is conserved to within a reciprocal lattice vector \mathbf{G}_{\parallel} , due to the abrupt potential change along the z axis the perpendicular momentum \mathbf{k}_{\perp} is not conserved across the sample surface (i.e., \mathbf{k}_{\perp} is not a good quantum number except than deeply into the solid, contrary to \mathbf{k}_{\parallel}). Thus, the surface can play a direct role in momentum conservation, delivering the necessary momentum for indirect transitions even in absence of the crystal potential (i.e., the so-called *surface photoelectric effect*; see also Eq. (12) and the related discussion).

Reverting to the three-step model *direct-transition* description of Fig. 4, the transmission through the sample surface is obtained by matching the bulk Bloch eigenstates

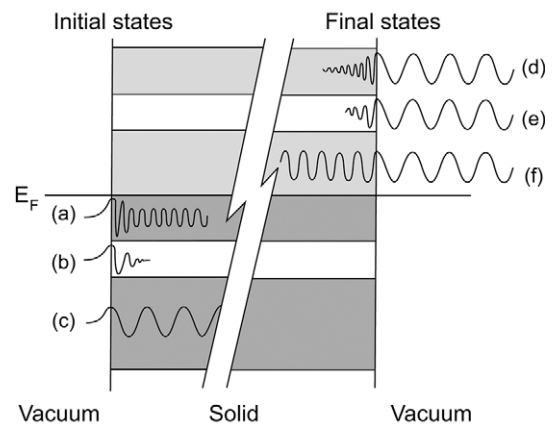


Fig. 2. Initial (left) and final (right) eigenstates for the semi-infinite crystal. Left: (a) surface resonance; (b) surface Shockley state situated in a gap of the bulk band structure; (c) bulk Bloch state. Right: (d) surface resonance; (e) in-gap evanescent state; (f) bulk Bloch final state (from Ref. [35]).

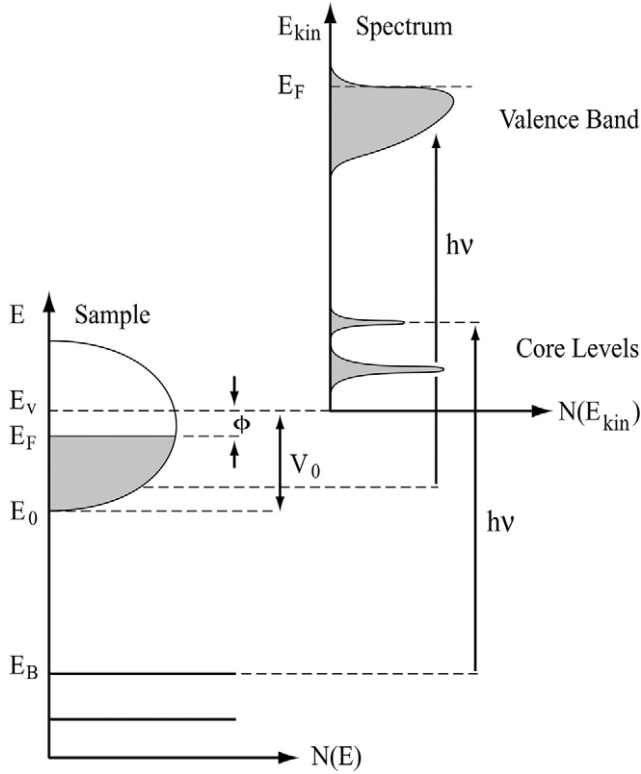


Fig. 3. Energetics of the photoemission process (from Ref. [17]). The electron energy distribution produced by the incoming photons, and measured as a function of the kinetic energy E_{kin} of the photoelectrons (right), is more conveniently expressed in terms of the binding energy E_B (left) when one refers to the density of states in the solid ($E_B = 0$ at E_F).

inside the sample to free-electron plane waves in vacuum. Because of the translational symmetry in the x - y plane across the surface, from these matching conditions it follows that the parallel component of the electron momentum is actually conserved in the process:

$$\mathbf{k}_{\parallel} = \mathbf{K}_{\parallel} = \frac{1}{\hbar} \sqrt{2mE_{kin}} \cdot \sin \vartheta \quad (7)$$

where \mathbf{k}_{\parallel} is the component parallel to the surface of the electron crystal momentum in the *extended-zone* scheme (upon going to larger ϑ angles, one actually probes electrons with \mathbf{k}_{\parallel} lying in higher-order Brillouin zones; by subtracting the corresponding reciprocal-lattice vector \mathbf{G}_{\parallel} , the *reduced* electron crystal momentum in the first Brillouin zone is obtained). As for the determination of \mathbf{k}_{\perp} , which is not conserved but is also needed in order to map the electronic dispersion $E(\mathbf{k})$ vs the total crystal wave vector \mathbf{k} , a different approach is required. As a matter of fact, several specific experimental methods for absolute three dimensional band mapping have been developed [17,38,39], which however are rather complex and require additional and/or complementary experimental data. Alternatively, the value of \mathbf{k}_{\perp} can be determined if some *a priori* assumption is made for the dispersion of the electron final states involved in the photoemission process; in particular, one can either use the results of band structure calculations, or adopt a nearly-free-electron description for the final bulk Bloch states:

$$E_f(\mathbf{k}) = \frac{\hbar^2 \mathbf{k}^2}{2m} - |E_0| = \frac{\hbar^2 (\mathbf{k}_{\parallel}^2 + \mathbf{k}_{\perp}^2)}{2m} - |E_0| \quad (8)$$

where once again the electron momenta are defined in the extended-zone scheme, and E_0 corresponds to the bottom of the valence band as indicated in Fig. 4 (note that both E_0 and E_f are referenced to the Fermi energy E_F , while E_{kin} is referenced to the vacuum level E_v). Because $E_f = E_{kin} + \phi$ and $\hbar^2 \mathbf{k}_{\parallel}^2 / 2m = E_{kin} \sin^2 \vartheta$, which follow from Fig. 4 and Eq. (7) one obtains from Eq. (8):

$$\mathbf{k}_{\perp} = \frac{1}{\hbar} \sqrt{2m(E_{kin} \cos^2 \vartheta + V_0)}. \quad (9)$$

Here $V_0 = |E_0| + \phi$ is the *inner potential*, which corresponds to the energy of the bottom of the valence band referenced to vacuum level E_v . From Eq. (9) and the measured values of E_{kin} and ϑ , if V_0 is also known, one can then obtain the corresponding value of \mathbf{k}_{\perp} . As for the determination of V_0 , three methods are generally used: (i) optimize the agreement between theoretical and experimental band mapping for the occupied electronic state; (ii) set V_0 equal to the theoretical zero of the muffin tin potential used in band structure calculations; (iii) infer V_0 from the experimentally observed periodicity of the dispersion $E(\mathbf{k}_{\perp})$. The latter is actually the most convenient method as the experiment can be realized by simply detecting the photoelectrons emitted along the surface normal (i.e., $\mathbf{K}_{\parallel} = 0$) while varying the incident photon energy and, in turn, the energy E_{kin} of the photoelectrons and thus \mathbf{K}_z (see Eq. (5)). Note that the nearly-free electron approximation for the final states is expected to work well for materials in which the Fermi surface has a simple spherical (free-electron-like) topology such as in the alkali metals, and for high-energy final states in which case the crystal potential is a small perturbation (eventually the final-state bands become so closely spaced in energy to form a continuum, and the details of the final states become unimportant). However this approximation is often used also for more complicated systems, even if the initial states are not free electron-like.

A particular case in which the uncertainty in \mathbf{k}_{\perp} is less relevant is that of the low-dimensional systems characterized by an anisotropic electronic structure and, in particular, a negligible dispersion along the z axis (i.e., the surface normal, see Fig. 6(a)). The electronic dispersion is then almost exclusively determined by \mathbf{k}_{\parallel} (as in the case of many transition metal oxides, such as for example the two-dimensional copper oxide superconductors [11]). As a result, one can map out in detail the electronic dispersion relations $E(\mathbf{k})$ simply by tracking, as a function of \mathbf{K}_{\parallel} , the

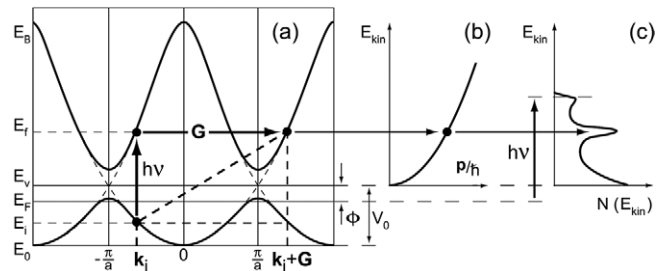


Fig. 4. Kinematics of the photoemission process within the three-step nearly-free-electron final state model: (a) direct optical transition in the solid (the lattice supplies the required momentum); (b) free-electron final state in vacuum; (c) corresponding photoelectron spectrum, with a background due to the scattered electrons ($E_B = 0$ at E_F). From Ref. [37].

energy position of the peaks detected in the ARPES spectra for different take-off angles (as in Fig. 6(b), where both direct and inverse photoemission spectra for a single band dispersing through the Fermi energy E_F are shown). Furthermore, as an additional bonus of the lack of z dispersion, one can directly identify the width of the photoemission peaks with the lifetime of the photohole [41], which contains information on the intrinsic correlation effects of the system and is formally described by the imaginary part of the electron self energy (see Section 4). On the contrary, in 3D systems the linewidth contains contributions from both photohole and photoelectron lifetimes, with the latter reflecting final state scattering processes and thus the finite probing depth; as a consequence, isolating the intrinsic many-body effects becomes a much more complicated problem.

What just discussed for the lifetime can be easily seen from the expression for the FWHM of an ARPES lineshape for a single nearly-free electron-like band [41]:

$$\Gamma = \frac{\Gamma_i/|v_{i\perp}| + \Gamma_f/|v_{f\perp}|}{|1/v_{i\perp}[1 - mv_{i\parallel} \sin^2 \vartheta/\hbar k_{\parallel}] - 1/v_{f\perp}[1 - mv_{f\parallel} \sin^2 \vartheta/\hbar k_{\parallel}]|}. \quad (10)$$

Here Γ_f and Γ_i are the inverse lifetime of photoelectron and photohole in the final and initial states, respectively, and v_i and v_f are the corresponding group velocities (e.g., $\hbar v_{i\perp} = \partial E_i / \partial k_{\perp}$). Note in particular that: (i) for initial states very close to E_F , $\Gamma_i \rightarrow 0$ and the linewidth reflects only the lifetime of the final state Γ_f ; (ii) Eq. (10) simplifies considerably in the case of a material characterized by a two dimensional electronic structure, for which $|v_{i\perp}| \simeq 0$: as a result, the final-state lifetime contribution vanishes:

$$\Gamma = \frac{\Gamma_i}{|1 - mv_{i\parallel} \sin^2 \vartheta/\hbar k_{\parallel}|} \equiv C \Gamma_i. \quad (11)$$

Furthermore, depending on the sign of $v_{i\parallel}$, the measured linewidth can be compressed or expanded with respect to the intrinsic value of the inverse lifetime Γ_i . The two limiting cases mentioned above are beautifully exemplified by the data from the three-dimensional system Ag(100) presented in Fig. 5 [40]. While the normal incidence spectrum is dominated by $\Gamma_f \gg \Gamma_i$ and is extremely broad, the grazing incidence data from a momentum space region characterized by $v_{i\perp} = 0$, $v_{i\parallel} < 0$ and large, and k_{\parallel} small (which result in a compression factor $C = 0.5$), exhibit a linewidth which is even narrower than the intrinsic inverse lifetime Γ_i . Note that this does not imply any fundamental violation of the basic principles of quantum mechanics, but is just a direct consequence of the kinematics constraints of the photoemission process.

3. Three-step model and sudden approximation

To develop a formal description of the photoemission process, one has to calculate the transition probability w_{fi} for an optical excitation between the N -electron ground

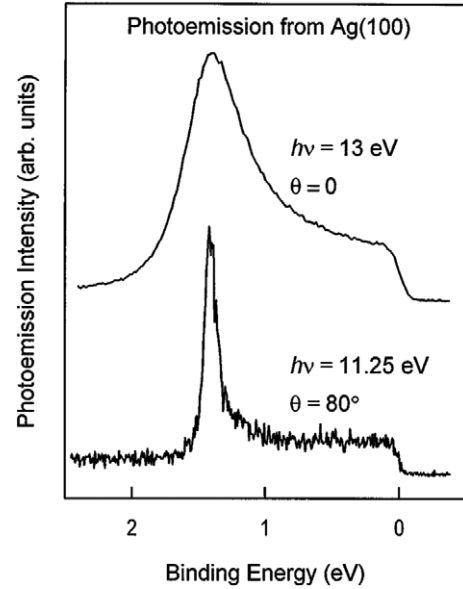


Fig. 5. Normal and grazing emission ARPES spectra from Ag(100) measured with photon energies specifically chosen to give rise to peaks with the same binding energy (from Ref. [40]).

state Ψ_i^N and one of the possible final states Ψ_f^N . This can be approximated by Fermi's golden rule:

$$w_{fi} = \frac{2\pi}{\hbar} |\langle \Psi_f^N | H_{int} | \Psi_i^N \rangle|^2 \delta(E_f^N - E_i^N - \hbar\nu) \quad (12)$$

where $E_i^N = E_i^{N-1} - E_B^k$ and $E_f^N = E_f^{N-1} + E_{kin}$ are the initial and final-state energies of the N -particle system (E_B^k is the binding energy of the photoelectron with kinetic energy E_{kin} and momentum \mathbf{k}). The interaction with the photon is treated as a perturbation given by:

$$H_{int} = \frac{e}{2mc} (\mathbf{A} \cdot \mathbf{p} + \mathbf{p} \cdot \mathbf{A}) = \frac{e}{mc} \mathbf{A} \cdot \mathbf{p} \quad (13)$$

where \mathbf{p} is the electronic momentum operator and \mathbf{A} is the electromagnetic vector potential (note that the gauge $\Phi = 0$ was chosen for the scalar potential Φ , and the quadratic term in \mathbf{A} was dropped because in the linear optical regime it is typically negligible with respect to the linear terms). In Eq. (13) we also made use of the commutator relation $[\mathbf{p}, \mathbf{A}] = -i\hbar \nabla \cdot \mathbf{A}$ and dipole approximation (i.e., \mathbf{A} constant over atomic dimensions and therefore $\nabla \cdot \mathbf{A} = 0$, which holds in the ultraviolet). Although this is a routinely used approximation, it should be noted that $\nabla \cdot \mathbf{A}$ might become important at the *surface* where the electromagnetic fields may have a strong spatial dependence. This surface photoemission contribution, which is proportional to $(\epsilon - 1)$ where ϵ is the medium dielectric function, can interfere with the bulk contribution resulting in asymmetric lineshapes for the bulk direct-transition peaks [14,42–44]. At this point, a more rigorous approach is to proceed with the so-called *one-step model* (Fig. 1(b)), in which photon absorption, electron removal, and electron detection are treated as a single coherent process [36,45–58]. In this case bulk, surface, and vacuum have to be included in the Hamiltonian describing the crystal, which implies that not only bulk states have to be considered but also surface and evanescent states, and surface resonances (see Fig. 2). Note that, under the assumption $\nabla \cdot \mathbf{A} = 0$, from Eq. (13) and the commutation relation $[H_0, \mathbf{p}] = i\hbar \nabla V$ (where

$H_0 = p^2/2m + V$ is the unperturbed Hamiltonian of the semi-infinite crystal) it follows that the matrix elements appearing in Eq. (12) are proportional to $\langle \Psi_f^N | \mathcal{A} \cdot \nabla V | \Psi_i^N \rangle$. This shows explicitly that for a true free-electron like system it would be impossible to satisfy simultaneously energy and momentum conservation laws inside the material because there $\nabla V = 0$. The only region where electrons could be photoexcited is at the surface where $\partial V/\partial z \neq 0$, which gives rise to the so-called *surface photoelectric effect*. However, due to the complexity of the one-step model, photoemission data are usually discussed within the three-step model (Fig. 1(a)), which although purely phenomenological has proven to be rather successful [49,59,60]. Within this approach, the photoemission process is subdivided into three independent and sequential steps:

- (i) Optical excitation of the electron in the *bulk*.
- (ii) Travel of the excited electron to the surface.
- (iii) Escape of the photoelectron into vacuum.

The total photoemission intensity is then given by the product of three independent terms: the total probability for the optical transition, the scattering probability for the travelling electrons, and the transmission probability through the surface potential barrier. Step (i) contains all the information about the intrinsic electronic structure of the material and will be discussed in detail below. Step (ii) can be described in terms of an effective mean free path, proportional to the probability that the excited electron will reach the surface without scattering (i.e., with no change in energy and momentum). The inelastic scattering processes, which determine the surface sensitivity of photoemission (see Section 6), give rise to a continuous background in the spectra which is usually ignored or subtracted. Step (iii) is described by a transmission probability through the surface, which depends on the energy of the excited electron and the material work function ϕ (in order to have any finite escape probability the condition $\hbar^2 \mathbf{k}_\perp^2/2m \geq |E_0| + \phi$ must be satisfied).

In evaluating step (i), and therefore the photoemission intensity in terms of the transition probability w_{fi} , it would be convenient to factorize the wavefunctions in Eq. (12) into photoelectron and $(N-1)$ -electron terms, as we have done for the corresponding energies. This however is far from trivial because during the photoemission process itself the system will relax. The problem simplifies within the *sudden approximation*, which is extensively used in many-body calculations of the photoemission spectra from interacting electron systems, and is in principle applicable only to high kinetic-energy electrons. In this limit, the photoemission process is assumed to be *sudden*, with no post-collisional interaction between the photoelectron and the system left behind (in other words, an electron is instantaneously removed and the effective potential of the system changes discontinuously at that instant). The final state Ψ_f^N can then be written as:

$$\Psi_f^N = \mathcal{A} \phi_f^k \Psi_f^{N-1} \quad (14)$$

where \mathcal{A} is an antisymmetric operator that properly antisymmetrizes the N -electron wavefunction so that the Pauli principle is satisfied, ϕ_f^k is the wavefunction of the

photoelectron with momentum \mathbf{k} , and Ψ_f^{N-1} is the final state wavefunction of the $(N-1)$ -electron system left behind, which can be chosen as an excited state with eigenfunction Ψ_m^{N-1} and energy E_m^{N-1} . The *total* transition probability is then given by the sum over *all* possible excited states m . Note, however, that the sudden approximation is inappropriate for low kinetic energy photoelectrons, which may need longer than the system response time to escape into vacuum. In this case, the so-called *adiabatic limit*, one can no longer factorize Ψ_f^N in two independent parts and the detailed screening of photoelectron and photohole has to be taken into account [62].

For the initial state, let us first assume for simplicity that Ψ_i^N is a single Slater determinant (i.e., Hartree–Fock formalism), so that we can write it as the product of a one-electron orbital ϕ_i^k and an $(N-1)$ -particle term:

$$\Psi_i^N = \mathcal{A} \phi_i^k \Psi_i^{N-1}. \quad (15)$$

More generally, however, Ψ_i^{N-1} should be expressed as $\Psi_i^{N-1} = c_k \Psi_i^N$, where c_k is the annihilation operator for an electron with momentum \mathbf{k} . This also shows that Ψ_i^{N-1} is *not* an eigenstate of the $(N-1)$ particle Hamiltonian, but is just what remains of the N -particle wavefunction after having pulled out one electron. At this point, we can write the matrix elements in Eq. (12) as:

$$\langle \Psi_f^N | H_{int} | \Psi_i^N \rangle = \langle \phi_f^k | H_{int} | \phi_i^k \rangle \langle \Psi_m^{N-1} | \Psi_i^{N-1} \rangle \quad (16)$$

where $\langle \phi_f^k | H_{int} | \phi_i^k \rangle \equiv M_{f,i}^k$ is the one-electron dipole matrix element, and the second term is the $(N-1)$ -electron overlap integral. Here, we replaced Ψ_f^{N-1} with an eigenstate Ψ_m^{N-1} , as discussed above. The total photoemission intensity measured as a function of E_{kin} at a momentum \mathbf{k} , namely $I(\mathbf{k}, E_{kin}) = \sum_{f,i} w_{f,i}$, is then proportional to:

$$\sum_{f,i} |M_{f,i}^k|^2 \sum_m |c_{m,i}|^2 \delta(E_{kin} + E_m^{N-1} - E_i^N - \hbar\nu) \quad (17)$$

where $|c_{m,i}|^2 = |\langle \Psi_m^{N-1} | \Psi_i^{N-1} \rangle|^2$ is the probability that the removal of an electron from state i will leave the $(N-1)$ -particle system in the excited state m . From here we see that, if $\Psi_i^{N-1} = \Psi_{m_0}^{N-1}$ for one particular $m = m_0$, the corresponding $|c_{m_0,i}|^2$ will be unity and all the others $c_{m,i}$ zero; in this case, if also $M_{f,i}^k \neq 0$, the ARPES spectra will be given by a delta function at the Hartree–Fock orbital energy $E_B^k = -\varepsilon_k$, as shown in Fig. 6(b) (i.e., non-interacting particle picture). In the strongly correlated systems, however, many of the $|c_{m,i}|^2$ will be different from zero because the removal of the photoelectron results in a strong change of the system effective potential and, in turn, Ψ_i^{N-1} will have an overlap with many of the eigenstates Ψ_m^{N-1} . Therefore, the ARPES spectra will not consist of single delta functions but will show a main line and several satellites according to the number of excited states m created in the process (Fig. 6(c)).

What discussed above is very similar to the situation encountered in photoemission from molecular hydrogen [63] in which not simply a single peak but many lines separated by few tenths of eV from each other are observed (solid line in Fig. 6(c), bottom right). These so-called ‘shake-up’ peaks correspond to the excitations of the different vibrational states of the H_2^+ molecule. In the case

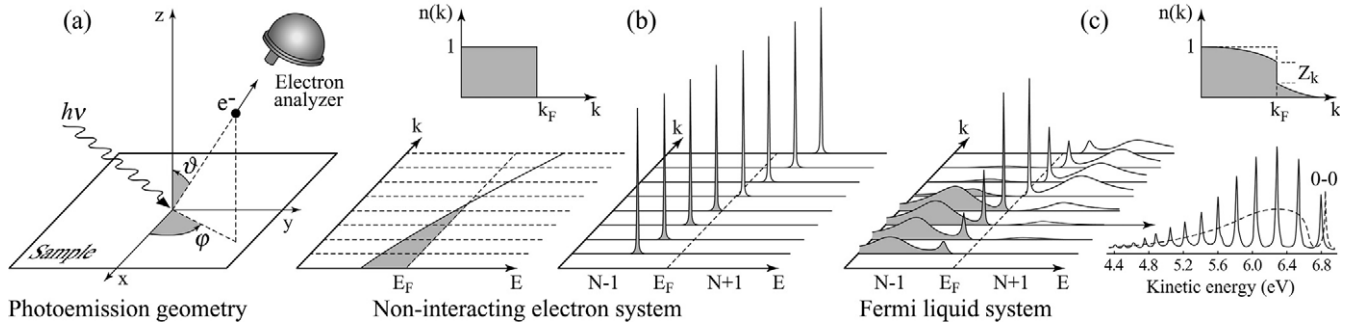


Fig. 6. (a) Geometry of an ARPES experiment; the emission direction of the photoelectron is specified by the polar (ϑ) and azimuthal (φ) angles. Momentum resolved one-electron removal and addition spectra for: (b) a non-interacting electron system (with a single energy band dispersing across the Fermi level); (c) an interacting Fermi liquid system. The corresponding ground-state ($T = 0$ K) momentum distribution function $n(\mathbf{k})$ is also shown. (c) Bottom right: photoelectron spectrum of gaseous hydrogen and ARPES spectrum of solid hydrogen developed from the gaseous one (from Ref. [11]).

of solid hydrogen (dashed line in Fig. 6(c), bottom right), as discussed by [61], the vibrational excitations would develop in a broad continuum while a sharp peak would be observed for the fundamental transition (from the ground state of the H_2 to the one of the H_2^+ molecule). Note that the fundamental line would also be the only one detected in the adiabatic limit, in which case the $(N - 1)$ -particle system is left in its ground state.

4. One-particle spectral function

In the discussion of photoemission on solids, and in particular on the correlated electron systems in which many $|c_{m,i}|^2$ in Eq. (17) are different from zero, the most powerful and commonly used approach is based on the Green's function formalism [64–69]. In this context, the propagation of a single electron in a many-body system is described by the *time-ordered* one-electron Green's function $\mathcal{G}(t - t')$, which can be interpreted as the probability amplitude that an electron added to the system in a Bloch state with momentum \mathbf{k} at a time zero will still be in the same state after a time $|t - t'|$. By taking the Fourier transform, $\mathcal{G}(t - t')$ can be expressed in energy-momentum representation resulting in $\mathcal{G}(\mathbf{k}, \omega) = G^+(\mathbf{k}, \omega) + G^-(\mathbf{k}, \omega)$, where $G^+(\mathbf{k}, \omega)$ and $G^-(\mathbf{k}, \omega)$ are the one-electron addition and removal Green's function, respectively. At $T = 0$:

$$G^\pm(\mathbf{k}, \omega) = \sum_m \frac{|\langle \Psi_m^{N\pm 1} | c_{\mathbf{k}}^\pm | \Psi_i^N \rangle|^2}{\omega - E_m^{N\pm 1} + E_i^N \pm i\eta} \quad (18)$$

where the operator $c_{\mathbf{k}}^+ = c_{\mathbf{k}\sigma}^\dagger$ ($c_{\mathbf{k}}^- = c_{\mathbf{k}\sigma}$) creates (annihilates) an electron with energy ω , momentum \mathbf{k} , and spin σ in the N -particle initial state Ψ_i^N , the summation runs over all possible $(N \pm 1)$ -particle eigenstates $\Psi_m^{N\pm 1}$ with eigenvalues $E_m^{N\pm 1}$, and η is a positive infinitesimal (note also that from here on we will take $\hbar = 1$). In the limit $\eta \rightarrow 0^+$ one can make use of the identity $(x \pm i\eta)^{-1} = \mathcal{P}(1/x) \mp i\pi\delta(x)$, where \mathcal{P} denotes the principle value, to obtain the *one-particle spectral function* $A(\mathbf{k}, \omega) = A^+(\mathbf{k}, \omega) + A^-(\mathbf{k}, \omega) = -(1/\pi) \text{Im } G(\mathbf{k}, \omega)$, with:

$$A^\pm(\mathbf{k}, \omega) = \sum_m |\langle \Psi_m^{N\pm 1} | c_{\mathbf{k}}^\pm | \Psi_i^N \rangle|^2 \delta(\omega - E_m^{N\pm 1} + E_i^N) \quad (19)$$

and $G(\mathbf{k}, \omega) = G^+(\mathbf{k}, \omega) + [G^-(\mathbf{k}, \omega)]^*$, which defines the *retarded* Green's function. Note that $A^-(\mathbf{k}, \omega)$ and $A^+(\mathbf{k}, \omega)$

define the one-electron removal and addition spectra which one can probe with direct and inverse photoemission, respectively. This is evidenced, for the direct case, by the comparison between the expression for $A^-(\mathbf{k}, \omega)$ and Eq. (17) for the photoemission intensity (note that in the latter $\Psi_i^{N-1} = c_{\mathbf{k}} \Psi_i^N$ and the energetics of the photoemission process has been explicitly accounted for). Finite temperatures effect can be taken into account by extending the Green's function formalism just introduced to $T \neq 0$ (see, e.g., Ref. [67]). In the latter case, by invoking once again the sudden approximation the intensity measured in an ARPES experiment on a 2D single-band system can be conveniently written as:

$$I(\mathbf{k}, \omega) = I_0(\mathbf{k}, \nu, \mathbf{A}) f(\omega) A(\mathbf{k}, \omega) \quad (20)$$

where $\mathbf{k} = \mathbf{k}_\parallel$ is the in-plane electron momentum, ω is the electron energy with respect to the Fermi level, and $I_0(\mathbf{k}, \nu, \mathbf{A})$ is proportional to the squared one-electron matrix element $|M_{f,i}^{\mathbf{k}}|^2$ and therefore depends on the electron momentum, and on the energy and polarization of the incoming photon. We also introduced the Fermi function $f(\omega) = (e^{\omega/k_B T} + 1)^{-1}$ which accounts for the fact that direct photoemission probes only the occupied electronic states. Note that in Eq. (20) we neglected the presence of any extrinsic background and the broadening due to the energy and momentum resolution, which however have to be carefully considered when performing a quantitative analysis of the ARPES spectra (see Section 5 and Eq. (27)).

The corrections to the Green's function originating from electron-electron correlations can be conveniently expressed in terms of the electron *proper self energy* $\Sigma(\mathbf{k}, \omega) = \Sigma'(\mathbf{k}, \omega) + i\Sigma''(\mathbf{k}, \omega)$. Its real and imaginary part contain all the information on the energy renormalization and lifetime, respectively, of an electron with band energy $\varepsilon_{\mathbf{k}}$ and momentum \mathbf{k} propagating in a many-body system. The Green's and spectral functions expressed in terms of the self energy are then given by:

$$G(\mathbf{k}, \omega) = \frac{1}{\omega - \varepsilon_{\mathbf{k}} - \Sigma(\mathbf{k}, \omega)}, \quad (21)$$

$$A(\mathbf{k}, \omega) = -\frac{1}{\pi} \frac{\Sigma''(\mathbf{k}, \omega)}{[\omega - \varepsilon_{\mathbf{k}} - \Sigma'(\mathbf{k}, \omega)]^2 + [\Sigma''(\mathbf{k}, \omega)]^2}. \quad (22)$$

Because $G(t, t')$ is a linear response function to an external perturbation, the real and imaginary parts of its Fourier

transform $G(\mathbf{k}, \omega)$ have to satisfy causality and, therefore, are related by Kramers–Kronig relations. This implies that if the full $A(\mathbf{k}, \omega) = -(1/\pi) \text{Im } G(\mathbf{k}, \omega)$ is available from photoemission and inverse photoemission, one can calculate $\text{Re } G(\mathbf{k}, \omega)$ and then obtain both the real and imaginary parts of the self energy directly from Eq. (21). However, due to the lack of high-quality inverse photoemission data, this analysis is usually performed only using ARPES spectra by taking advantage of certain approximations (such as, e.g., particle-hole symmetry within a narrow energy range about E_F [70]).

In general, the exact calculation of $\Sigma(\mathbf{k}, \omega)$ and, in turn, of $A(\mathbf{k}, \omega)$ is an extremely difficult task. In the following, as an example we will briefly consider the interacting FL case [71–73]. Let us start from the trivial $\Sigma(\mathbf{k}, \omega) = 0$ non-interacting case. The N -particle eigenfunction Ψ^N is a single Slater determinant and we always end up in a single eigenstate when removing or adding an electron with momentum \mathbf{k} . Therefore, $G(\mathbf{k}, \omega) = 1/(\omega - \varepsilon_k \pm i\eta)$ has only one pole for each \mathbf{k} , and $A(\mathbf{k}, \omega) = \delta(\omega - \varepsilon_k)$ consists of a single line at the band energy ε_k (as shown in Fig. 6(b)). In this case, the occupation numbers $n_{\mathbf{k}\sigma} = c_{\mathbf{k}\sigma}^\dagger c_{\mathbf{k}\sigma}$ are good quantum numbers and for a metallic system the *momentum distribution* (i.e., the expectation value $n(\mathbf{k}) \equiv \langle n_{\mathbf{k}\sigma} \rangle$, quite generally independent of the spin σ for nonmagnetic systems), is characterized by a sudden drop from 1 to 0 at $\mathbf{k} = \mathbf{k}_F$ (Fig. 6(b), top), which defines a sharp Fermi surface. If we now switch on the electron-electron correlation adiabatically, (so that the system remains at equilibrium), any particle added into a Bloch state has a certain probability of being scattered out of it by a collision with another electron, leaving the system in an excited state in which additional electron-hole pairs have been created. The momentum distribution $n(\mathbf{k})$ will now show a discontinuity smaller than 1 at \mathbf{k}_F and a finite occupation probability for $\mathbf{k} > \mathbf{k}_F$ even at $T = 0$ (Fig. 6(c), top). As long as $n(\mathbf{k})$ shows a finite discontinuity $Z_k > 0$ at $\mathbf{k} = \mathbf{k}_F$, we can describe the correlated Fermi sea in terms of well defined *quasiparticles*, i.e., electrons *dressed* with a manifold of excited states, which are characterized by a pole structure similar to the one of the non-interacting system but with renormalized energy ε_k and mass m^* , and a finite lifetime $\tau_k = 1/\Gamma_k$. In other words, the properties of a FL are similar to those of a free electron gas with damped quasiparticles. As the bare-electron character of the quasiparticle or pole strength (also called coherence factor) is $Z_k < 1$ and the total spectral weight must be conserved (see Eq. (25)), we can separate $G(\mathbf{k}, \omega)$ and $A(\mathbf{k}, \omega)$ into a *coherent* pole part and an *incoherent* smooth part without poles [74]:

$$G(\mathbf{k}, \omega) = \frac{Z_k}{\omega - \varepsilon_k + i\Gamma_k} + G_{\text{inch}}, \quad (23)$$

$$A(\mathbf{k}, \omega) = Z_k \frac{\Gamma_k/\pi}{(\omega - \varepsilon_k)^2 + \Gamma_k^2} + A_{\text{inch}}, \quad (24)$$

where

$$Z_k = (1 - \partial\Sigma'/\partial\omega)^{-1}, \quad \varepsilon_k = Z_k(\varepsilon_k + \Sigma'), \quad \Gamma_k = Z_k|\Sigma''|,$$

and the self energy and its derivatives are evaluated at $\omega = \varepsilon_k$. It should be emphasized that the FL description is

valid only in proximity to the Fermi surface and rests on the condition $\varepsilon_k - \mu \gg |\Sigma''|$ for small $(\omega - \mu)$ and $(\mathbf{k} - \mathbf{k}_F)$. Furthermore, $\Gamma_k \propto [(\pi k_B T)^2 + (\varepsilon_k - \mu)^2]$ for a FL system in two or more dimensions [74,75], although additional logarithmic corrections should be included in the two-dimensional case [76]. By comparing the electron removal and addition spectra for a FL of quasiparticles with those of a non-interacting electron system (in the lattice periodic potential), the effect of the self-energy correction becomes evident (see Fig. 6(c) and (b), respectively). The quasiparticle peak has now a finite lifetime (due to Σ''), and it sharpens up rapidly thus emerging from the broad incoherent component upon approaching the Fermi level, where the lifetime is infinite corresponding to a well defined quasiparticle [note that the coherent and incoherent part of $A(\mathbf{k}, \omega)$ represent the main line and satellite structure discussed in the previous section and shown in Fig. 6(c), bottom right]. Furthermore, the peak position is shifted with respect to the bare band energy ε_k (due to Σ'): as the quasiparticle mass is larger than the band mass because of the dressing ($m^* > m$), the total dispersion (or bandwidth) will be smaller ($|\varepsilon_k| < |\varepsilon_k|$).

Among the general properties of the spectral function there are also several sum rules. A fundamental one, which in discussing the FL model was implicitly used to state that $\int d\omega A_{\text{ch}} = Z_k$ and $\int d\omega A_{\text{inch}} = 1 - Z_k$ (where A_{ch} and A_{inch} refer to coherent and incoherent parts of the spectral function, respectively), is the following:

$$\int_{-\infty}^{+\infty} d\omega A(\mathbf{k}, \omega) = 1 \quad (25)$$

which reminds us that $A(\mathbf{k}, \omega)$ describes the probability of removing/adding an electron with momentum \mathbf{k} and energy ω to a many-body system. However, as it also requires the knowledge of the electron addition part of the spectral function, it is not so useful in the analysis of ARPES data. A sum rule more relevant to this task is:

$$\int_{-\infty}^{+\infty} d\omega f(\omega) A(\mathbf{k}, \omega) = n(\mathbf{k}) \quad (26)$$

which solely relates the one-electron removal spectrum to the momentum distribution $n(\mathbf{k})$. When electronic correlations are important and the occupation numbers are no longer good quantum numbers, the discontinuity at \mathbf{k}_F is reduced (as discussed for the FL case) but a drop in $n(\mathbf{k})$ is usually still observable even for strong correlations [78]. By tracking in k -space the *loci* of steepest descent of the experimentally determined $n(\mathbf{k})$, i.e., maxima in $|\nabla_k n(\mathbf{k})|$, one may thus identify the Fermi surface even in those correlated systems exhibiting particularly complex ARPES features. However, great care is necessary in making use of Eq. (26) because the integral of Eq. (20) does not give just $n(\mathbf{k})$ but rather $I_0(\mathbf{k}, \nu, A)n(\mathbf{k})$ [11].

5. Matrix elements and finite resolution effects

As discussed in the previous section and summarized by Eq. (20), ARPES directly probes the one-particle spectral function $A(\mathbf{k}, \omega)$. However, in extracting quantitative information from the experiment, not only the effect of

the matrix element term $I_0(\mathbf{k}, \nu, \mathbf{A})$ has to be taken into account, but also the finite experimental resolution and the extrinsic continuous background due to the secondaries (those electrons which escape from the solid after having suffered inelastic scattering events and, therefore, with a reduced E_{kin}). The latter two effects may be explicitly accounted for by considering a more realistic expression for the photocurrent $I(\mathbf{k}, \omega)$:

$$\int d\tilde{\omega} d\tilde{\mathbf{k}} I_0(\tilde{\mathbf{k}}, \nu, \mathbf{A}) f(\tilde{\omega}) A(\tilde{\mathbf{k}}, \tilde{\omega}) R(\omega - \tilde{\omega}) Q(\mathbf{k} - \tilde{\mathbf{k}}) + B \quad (27)$$

which consists of the convolution of Eq. (20) with energy (R) and momentum (Q) resolution functions (R is typically a Gaussian, Q may be more complicated), and of the background correction B . Of the several possible forms for the background function B [17], two are more frequently used: (i) the step-edge background (with three parameters for height, energy position, and width of the step-edge), which reproduces the background observed all the way to E_F in an unoccupied region of momentum space; (ii) the Shirley background $B_{Sh}(\omega) \propto \int_{\omega}^{\mu} d\omega' P(\omega')$, which allows to extract from the measured photocurrent $I(\omega) = P(\omega) + c_{Sh} B_{Sh}(\omega)$ the contribution $P(\omega)$ of the unscattered electrons (with only the parameter c_{Sh} [79]).

Let us now very briefly illustrate the effect of the matrix element term $I_0(\mathbf{k}, \nu, \mathbf{A}) \propto |M_{f,i}^k|^2$, which is responsible for the dependence of the photoemission data on photon energy and experimental geometry, and may even result in complete suppression of the intensity [80–83]. By using the commutation relation $\hbar \mathbf{p}/m = -i[\mathbf{x}, H]$, we can write $|M_{f,i}^k|^2 \propto |\langle \phi_f^k | \varepsilon \cdot \mathbf{x} | \phi_i^k \rangle|^2$, where ε is a unit vector along the polarization direction of the vector potential \mathbf{A} . As in Fig. 7(a), let us consider photoemission from a $d_{x^2-y^2}$ orbital, with the detector located in the mirror plane (when the detector is out of the mirror plane, the problem is more complicated because of the lack of an overall well defined even/odd symmetry). In order to have non vanishing photoemission intensity, the whole integrand in the overlap integral must be an even function under reflection with respect to the mirror plane. Because odd parity final states would be zero everywhere on the mirror plane and therefore also at the detector, the final state wavefunction ϕ_f^k itself must be even. In particular, at the detector the photoelectron is described by an even parity plane-wave state $e^{i\mathbf{k}\cdot\mathbf{r}}$ with momentum in the mirror plane and fronts orthogonal to it [82]. In turn, this implies that $(\varepsilon \cdot \mathbf{x})|\phi_i^k\rangle$ must be even. In the case depicted in Fig. 7(a) where $|\phi_i^k\rangle$ is also even, the photoemission process is symmetry allowed for \mathbf{A} even or in-plane (i.e., $\varepsilon_p \cdot \mathbf{x}$ depends only on in-plane coordinates and is therefore even under reflection with respect to the plane) and forbidden for \mathbf{A} odd or normal to the mirror plane (i.e., $\varepsilon_s \cdot \mathbf{x}$ is odd as it depends on normal-to-the-plane coordinates). For a generic initial state of either even or odd symmetry with respect to the mirror plane, the polarization conditions resulting in an overall even matrix element can be summarized as:

$$\langle \phi_f^k | \mathbf{A} \cdot \mathbf{p} | \phi_i^k \rangle \begin{cases} \phi_i^k \text{ even } \langle + | + \rangle \Rightarrow \mathbf{A} \text{ even} \\ \phi_i^k \text{ odd } \langle + | - \rangle \Rightarrow \mathbf{A} \text{ odd.} \end{cases} \quad (28)$$

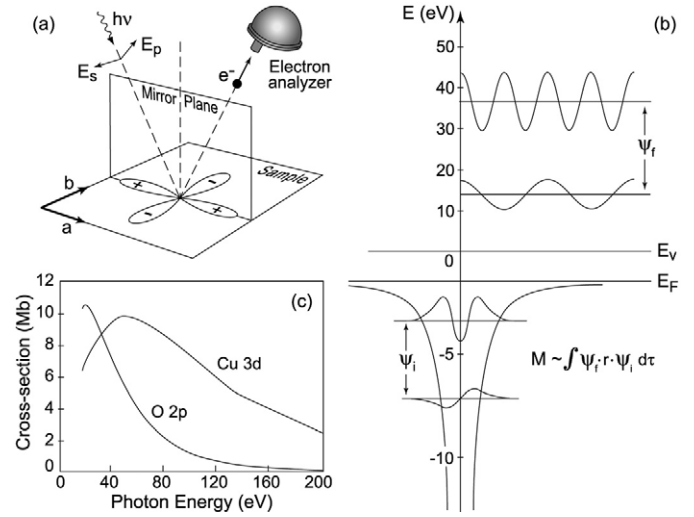


Fig. 7. (a) Mirror plane emission from a $d_{x^2-y^2}$ orbital. (b) Sketch of the optical transition between atomic orbitals with different angular momenta (the harmonic oscillator wavefunctions are here used for simplicity) and free electron wavefunctions with different kinetic energies (from Ref. [17]). (c) Calculated photon energy dependence of the photoionization cross-sections for Cu 3d and O 2p atomic levels (from Ref. [77]).

In order to discuss the photon energy dependence, from Eq. (13) and by considering a plane wave $e^{i\mathbf{k}\cdot\mathbf{r}}$ for the photoelectron at the detector, one may more conveniently write $|M_{f,i}^k|^2 \propto |(\varepsilon \cdot \mathbf{k}) \langle \phi_f^k | e^{i\mathbf{k}\cdot\mathbf{r}} | \phi_i^k \rangle|^2$. The overlap integral, as sketched in Fig. 7(b), strongly depends on the details of the initial state wavefunction (peak position of the radial part and oscillating character of it), and on the wavelength of the outgoing plane wave. Upon increasing the photon energy, both E_{kin} and \mathbf{k} increase, and $M_{f,i}^k$ changes in a non-necessarily monotonic fashion (see Fig. 7(c), for the Cu 3d and the O 2p atomic case). In fact, the photoionization cross section is usually characterized by one minimum in free atoms, the so-called Cooper minimum [84], and a series of them in solids [85].

6. State-of-the-art photoemission

The configuration of a generic angle-resolved photoemission beamline is shown in Fig. 8. A beam of white radiation is produced in a wiggler or an undulator (these so-called ‘insertion devices’ are the straight sections of the electron storage ring where radiation is produced): the light is then monochromatized at the desired photon energy by a grating monochromator, and is focused on the sample. Alternatively, a gas-discharge lamp can be used as a radiation source (once properly monochromatized, to avoid complications due to the presence of different satellites and refocused to a small spot size, essential for high angular resolution). However, synchrotron radiation offers important advantages: it covers a wide spectral range (from the visible to the X-ray region) with an intense and highly polarized continuous spectrum, while a discharge lamp provides only a few resonance lines at discrete energies. Photoemitted electrons are then collected by the analyzer, where kinetic energy and emission angle are determined (the whole system is in ultra-high vacuum at pressures lower than 5×10^{-11} torr).

A conventional hemispherical analyzer consists of a multi-element electrostatic input lens, a hemispherical

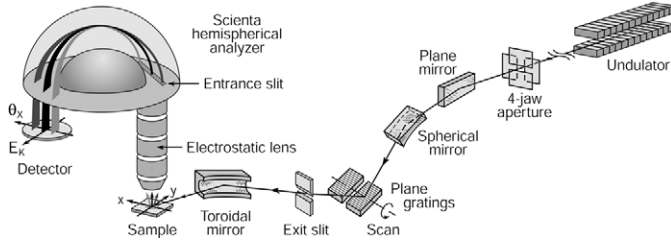


Fig. 8. Beamline equipped with a plane grating monochromator and a 2D position-sensitive electron analyzer.

deflector with entrance and exit slits, and an electron detector (i.e., a channeltron or a multi-channel detector). The heart of the analyzer is the deflector which consists of two concentric hemispheres (of radius R_1 and R_2). These are kept at a potential difference ΔV , so that only those electrons reaching the entrance slit with kinetic energy within a narrow range centered at $E_{pass} = e\Delta V/(R_1/R_2 - R_2/R_1)$ will pass through this hemispherical capacitor, thus reaching the exit slit and then the detector. This way it is possible to measure the kinetic energy of the photoelectrons with an energy resolution given by $\Delta E_a = E_{pass}(w/R_0 + \alpha^2/4)$, where $R_0 = (R_1 + R_2)/2$, w is the width of the entrance slit, and α is the acceptance angle. The role of the electrostatic lens is that of decelerating and focusing the photoelectrons onto the entrance slit. By scanning the lens retarding potential one can effectively record the photoemission intensity versus the photoelectron kinetic energy. One of the innovative characteristics of the state-of-the-art analyzer is the two-dimensional position-sensitive detector consisting of two micro-channel plates and a phosphor plate in series, followed by a CCD camera. In this case, no exit slit is required: the electrons, spread apart along the Y axis of the detector (Fig. 8) as a function of their kinetic energy due to the travel through the hemispherical capacitor, are detected simultaneously (in other words, a range of electron energies is dispersed over one dimension of the detector and can be measured in parallel; scanning the lens voltage is in principle no longer necessary, at least for narrow energy windows (a few percent of E_{pass})). Furthermore, contrary to a conventional electron spectrometer in which the momentum information is averaged over all the photoelectrons within the acceptance angle (typically $\pm 1^\circ$), state-of-the-art 2D position-sensitive electron analyzers can be operated in angle-resolved mode, which provides energy-momentum information not only at a single k -point but along an extended cut in k -space. In particular, the photoelectrons within an angular window of $\sim 14^\circ$ along the direction defined by the analyzer entrance slit are focused on different X positions on the detector (Fig. 8). It is thus possible to measure multiple energy distribution curves simultaneously for different photoelectron angles, obtaining a 2D snapshot of energy versus momentum (Fig. 9).

State-of-the-art spectrometers typically allow for energy and angular resolutions of approximately a few meV and 0.2° , respectively. Taking as example the transition metal oxides and in particular the cuprate superconductors (for which $2\pi/a \simeq 1.6 \text{ \AA}^{-1}$), one can see from Eq. (7) that 0.2° corresponds to $\sim 0.5\%$ of the Brillouin zone size, for the 21.2 eV photons of the HeI α line typically used in ARPES systems equipped with a gas-discharge lamp. In the case of

a beamline, to estimate the total energy resolution one has to take into account also ΔE_m of the monochromator, which can be adjusted with entrance and exit slits (the ultimate resolution a monochromator can deliver is given by its resolving power $R = E/\Delta E_m$; it can be as good as 1–2 meV for 20 eV photons but worsens upon increasing the photon energy). To maximize the signal intensity at the desired total ΔE , monochromator and analyzer should be operated at comparable resolutions. As for the momentum resolution $\Delta k_{||}$, note that from Eq. (7) and neglecting the contribution due to the finite energy resolution one can write:

$$\Delta k_{||} \simeq \sqrt{2mE_{kin}/\hbar^2} \cdot \cos \vartheta \cdot \Delta \vartheta \quad (29)$$

where $\Delta \vartheta$ is the finite acceptance angle of the electron analyzer. From Eq. (29) it is clear that the momentum resolution is better at lower photon energy (i.e., lower E_{kin}), and larger polar angles ϑ (one can effectively improve the momentum resolution by extending the measurements to momenta outside the first Brillouin zone).

Because at lower photon energies it is possible to achieve higher energy and momentum resolution, most of the ARPES experiments are performed in the ultraviolet (typically for $h\nu < 100 \text{ eV}$). An additional advantage is that at low photon energies one can disregard the photon momentum $k_{hv} = 2\pi/\lambda$ in Eq. (7), as for 100 eV photons the momentum is 0.05 \AA^{-1} (only 3% of the Brillouin zone size, by taking again the cuprates as an example), and at 21.2 eV (HeI α) it is only 0.008 \AA^{-1} (0.5% of the zone). If on the contrary the photon momentum is not negligible, the photoemission process does not involve vertical transitions and κ must be explicitly taken into account in Eq. (7). For example, for 1487 eV photons (the Al K α line commonly used in X-ray photoemission) $k_{hv} \simeq 0.76 \text{ \AA}^{-1}$, which corresponds to 50% of the zone size.

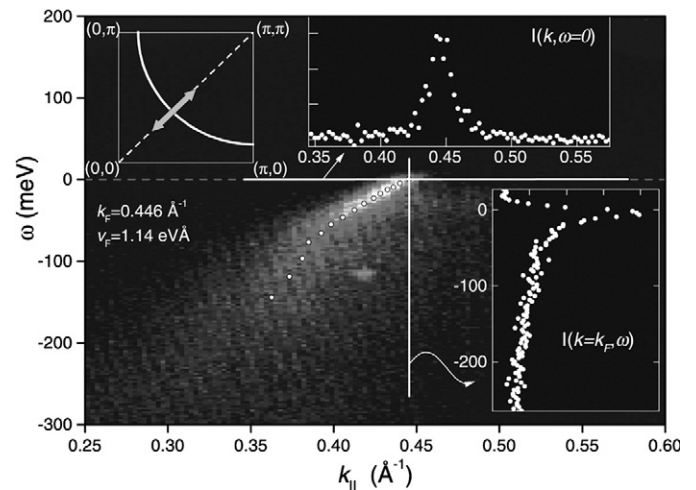


Fig. 9. Energy (ω) versus momentum ($k_{||}$) image plot of the photoemission intensity from $\text{Bi}_2\text{Sr}_2\text{CaCu}_2\text{O}_{8+\delta}$ along $(0, 0) - (\pi, \pi)$. This k -space cut was taken across the Fermi surface (see sketch of the 2D Brillouin zone) and allows a direct visualization of the photohole spectral function $A(k, \omega)$ (weighted by Fermi distribution and matrix elements): the quasiparticle dispersion can be followed up to E_F , as emphasized by the white circles. Energy scans at constant momentum (right) and momentum scans at constant energy (top) define energy distribution curves (EDCs) and momentum distribution curves (MDCs). From Ref. [36].

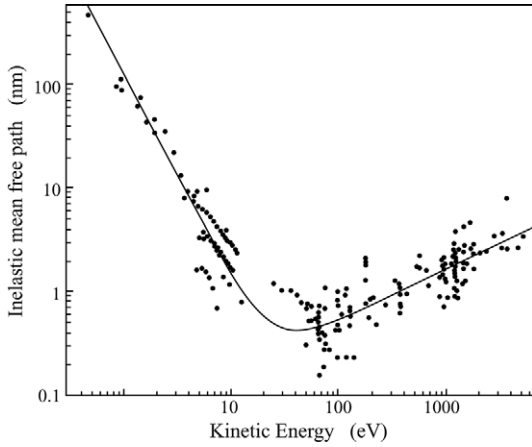


Fig. 10. Kinetic energy dependence of the “universal” mean free path for excited electrons in solids (from Ref. [87]).

A major drawback of working at low photon energies is the extreme surface sensitivity. As shown in Fig. 10, the mean free path for unscattered photoelectrons is characterized by a minimum of approximately 5 \AA at 20–100 eV kinetic energies [87], which are typical values in ARPES experiments. This means that a considerable fraction of the total photoemission intensity will be representative of the topmost surface layer, especially on systems characterized by a large structural/electronic anisotropy. Therefore, ARPES experiments have to be performed on atomically clean and well-ordered systems, which implies that atomically *fresh* and *flat* surfaces have to be “prepared” immediately prior to the experiment in ultra-high vacuum conditions (typically at pressures lower than 5×10^{-11} torr). Even then, however, because of the lower atomic coordination at the surface, the coexistence of bulk and surface electronic states, and the possible occurrence of chemical and/or structural surface instabilities, photoemission data may not always be representative of the intrinsic bulk electronic structure. In order to address this issue, great care has to be taken also over the structural and chemical characterization of the sample surface, which can be done independently by low-energy electron diffraction (LEED) and core-level X-ray photoemission spectroscopy (XPS), respectively (either prior to or during the ARPES experiments). In this regard it has to be emphasized that, although the ultimate resolutions are not as good as in the UV regime, the sensitivity to bulk over surface electronic states can be enhanced (see Fig. 10) by performing the ARPES experiments in the soft X-ray regime (500–1500 eV). The significance of this approach is well exemplified by recent angle-integrated resonance photoemission experiments performed on Ce compounds [88]. These Kondo systems are characterized by a very different degree of hybridization between the 4f electronic states and other valence bands: the hybridization is stronger the larger the Kondo temperature T_K . However, although CeRu_2Si_2 and CeRu_2 are characterized by very different T_K (approximately 22 and 1000 K, respectively), earlier photoemission studies reported similar spectra for the Ce 4f electronic states. By performing angle-integrated high resolution photoemission experiments at the 3d-4f ($h\nu \simeq 880 \text{ eV}$, $\Delta E \simeq 100 \text{ meV}$) and 4d-4f ($h\nu \simeq 120 \text{ eV}$, $\Delta E \simeq 50 \text{ meV}$) resonances (see Fig. 11), it was observed

that, while the spectra for the two compounds are indeed qualitatively similar at 120 eV photon energy, they are remarkably different at 880 eV. As the photoelectron mean free path increases from approximately 5 to almost 20 \AA upon increasing the photon energy from 120 to 880 eV (Fig. 10), it was concluded that the 4d-4f spectra mainly reflect the surface 4f electronic states. These are different from those of the bulk and are not representative of the intrinsic electronic properties of the two compounds, which are more directly probed at 880 eV: the 3d-4f spectra show a prominent structure corresponding to the tail of a Kondo peak in CeRu_2Si_2 , and a broader feature reflecting the more itinerant character of the 4f electrons in CeRu_2 [88].

In the following, we will move on to the review of recent ARPES results from several materials, such as Sr_2RuO_4 , $2H\text{-NbSe}_2$, $\text{Be}(0001)$, and $\text{Mo}(110)$. These examples will be used to illustrate the capability of this technique and some of the specific issues that one can investigate in detail by ARPES. In particular, these test cases will demonstrate that, by taking full advantage of the momentum and energy resolution as well as of the photon energy range nowadays available, state-of-the-art ARPES is a unique tool for *momentum space microscopy*.

6.1. Sr_2RuO_4 : Bands and Fermi surface

To illustrate how one can study electronic bands and Fermi surfaces by ARPES, and how critical the improvement in resolution has been in this regard, the novel superconductor Sr_2RuO_4 is a particularly good example. Its low-energy electronic structure, as predicted by band-structure calculations is characterized by three bands crossing the chemical potential [91,92]. These define a complex Fermi surface comprised of two electron pockets and one hole pocket (Fig. 12(d)), which have been clearly observed in de Haas–van Alphen experiments [93,94]. On the other hand, early photoemission measurements suggested a different topology [95–97], which generated a certain degree of controversy in the field [98]. This issue was conclusively resolved only by taking advantage of the

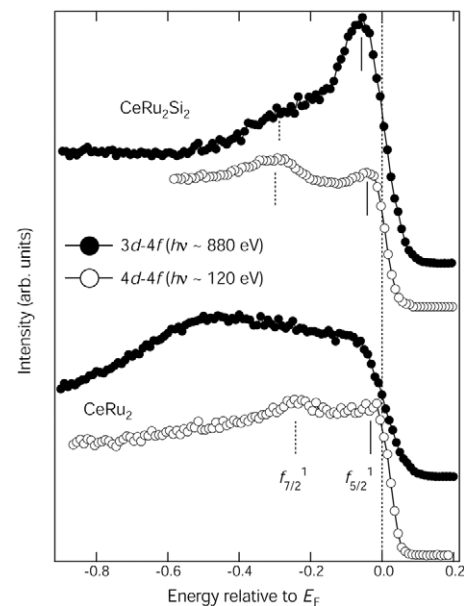


Fig. 11. High energy angle-integrated resonance photoemission data from Ce compounds at $T = 20 \text{ K}$ (from Ref. [88]).

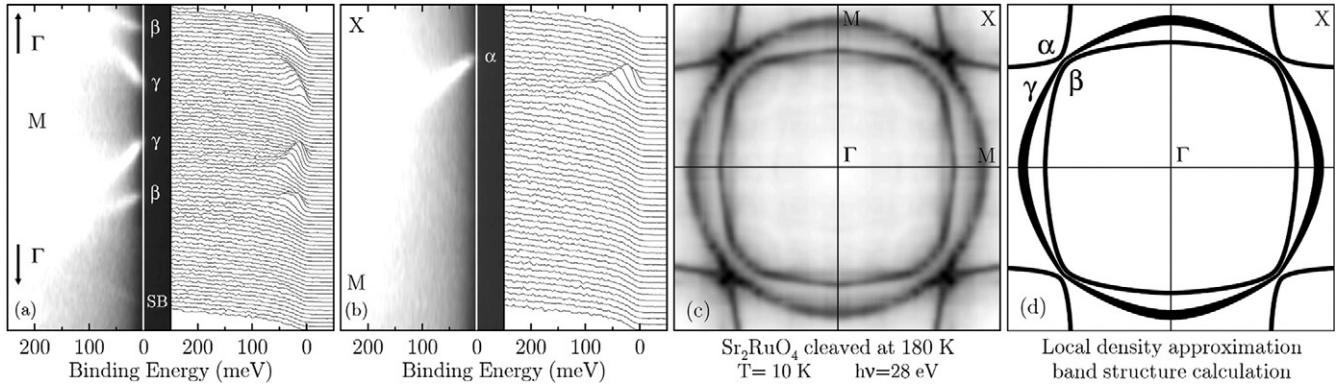


Fig. 12. ARPES spectra and corresponding intensity plot from Sr_2RuO_4 along (a) Γ -M, and (b) M-X. (c) Measured and (d) calculated [89] Fermi surface. All data were taken at 10 K on a Sr_2RuO_4 single crystal cleaved at 180 K (from Ref. [90]).

high energy and momentum resolution of the “new generation” of ARPES data: it was then recognized that a surface reconstruction [99] and, in turn, the detection of several direct and folded surface bands were responsible for the conflicting interpretations [90,100–102]. Figure 12(a) and (b) show high resolution ARPES data ($\Delta E = 14$ meV, $\Delta k = 1.5\%$ of the zone edge) taken at 10 K with 28 eV photons on a Sr_2RuO_4 single crystal cleaved at 180 K (for Sr_2RuO_4 , as recently discovered, high-temperature cleaving suppresses the reconstructed-surface contributions to the photoemission signal and allows one to isolate the bulk electronic structure [90]). Many well defined quasiparticle peaks disperse towards the Fermi energy and disappear upon crossing E_F . A Fermi energy intensity map (Fig. 12(c)) can then be obtained by integrating the spectra over a narrow energy window about $E_F(\pm 10$ meV). As the spectral function (multiplied by the Fermi function) reaches its maximum at E_F when a band crosses the Fermi energy, the Fermi surface is identified by the local maxima of the intensity map. Following this method, the three sheets of Fermi surface are clearly resolved and are in excellent agreement with the theoretical calculations (Fig. 12(d)).

6.2. $2H\text{-NbSe}_2$: Superconducting gap

$2H\text{-NbSe}_2$ is an interesting quasi two-dimensional system exhibiting a charge-density wave phase transition at approximately 33 K, and a phonon-mediated superconducting phase transition at 7.2 K. As indicated by band structure calculations [103], the valence-band electronic structure is characterized by a manifold of dispersive bands in a 6 eV range below the Fermi energy. At low energy, three dispersive bands are expected to cross the chemical potential and define three sheets of Fermi surface in the hexagonal Brillouin zone. Both the band manifold and the Fermi surface topology have been studied in great detail by ARPES; exception made for a weak energy renormalization, the normal-state experimental data are in extremely good agreement with the results of theoretical calculations (as shown in Fig. 13, where ARPES spectra and band structure calculations are compared for the Γ -K high symmetry direction). As for the low temperature charge-density wave phase, despite the intense effort no agreement has been reached yet on the driving force responsible for the transition [37,104].

Owing to the great improvement in energy and momentum resolution, it has now become possible to study by ARPES also the momentum and temperature dependence of the superconducting gap on low- T_c materials (until recently, experiments of this kind could be performed only for the much larger d-wave gap of the high- T_c superconductors [11]). The data presented in Fig. 14, which are one of the most impressive examples of combined high energy and momentum resolution in ARPES experiments on solid samples (i.e., $\Delta E = 2.5$ meV and $\Delta k = 0.2^\circ$), provide direct evidence for Fermi surface sheet-dependent superconductivity in $2H\text{-NbSe}_2$ [106]. A superconducting gap of about 1 meV was successfully detected along two of the normal-state Fermi surface sheets, but not along the third one. In fact, the opening of the gap is directly evidenced in Fig. 14(b) and (c) by the shift to high binding energies of the 5.3 K spectra leading-edge midpoint (which is instead located at E_F at 10 K, as expected for a metal), and by the simultaneous appearance of a peak below E_F (which reflects the piling up of the density of states due to the gap opening). This behavior is absent for the inner Fermi surface pocket (Fig. 14(a)).

6.3. Self energy and collective modes

As discussed in Section 4, the introduction of the electron self energy $\Sigma(\mathbf{k}, \omega) = \Sigma'(\mathbf{k}, \omega) + i\Sigma''(\mathbf{k}, \omega)$ is a powerful way to account for many-body correlations in solids. Its real and imaginary parts correspond, respectively, to the

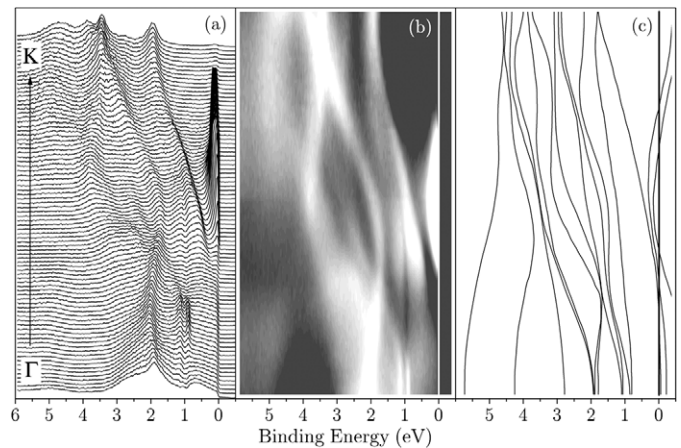


Fig. 13. (a) $2H\text{-NbSe}_2$ ARPES spectra (measured at 20 K with 21.2 eV photons), (b) corresponding image plot, and (c) band structure calculations along Γ -K (from Ref. [105]).

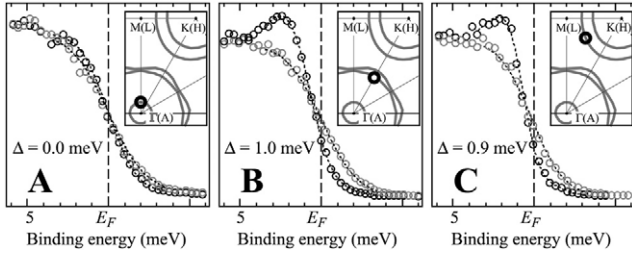


Fig. 14. Normal (10 K, gray) and superconducting state (5.3 K, black) ARPES spectra from 2H-NbSe₂, measured at k -points belonging to the three different sheets of Fermi surface (see insets). The value of the superconducting gap obtained by fitting the arpes data is indicated in each panel (from Ref. [106]).

energy renormalization with respect to the bare band energy ε_k and to the finite lifetime of the quasiparticles in the interacting system. Owing to the energy and momentum resolution nowadays achievable, both components of the self energy can be in principle estimated very accurately from the analysis of the ARPES intensity in terms of *energy distribution curves* (EDCs) and/or *momentum distribution curves* (MDCs), which is one of the aspects that make ARPES such a powerful tool for the investigation of complex materials. In some cases the MDC analysis may be more effective than the analysis of the EDCs in extracting information on the self energy. In fact, EDCs are typically characterized by a complex lineshape (Fig. 9) because of the nontrivial ω dependence of the self energy, the presence of additional background, and the low-energy cutoff due to the Fermi function. Furthermore, as evidenced by the generic expression for the spectral function $A(\mathbf{k}, \omega)$ in Eq. (22), the EDC peak position is determined by $\Sigma'(\mathbf{k}, \omega)$ as well as $\Sigma''(\mathbf{k}, \omega)$, because both terms are strongly energy dependent. On the other hand, if the self energy is independent of k normal to the Fermi surface (and the matrix elements are a slowly-varying function of k), then the corresponding MDCs are Lorentzians centered at $k = k_F + [\omega - \Sigma'(\omega)]/v_F^0$ with FWHM given by $2\Sigma''(\omega)/v_F^0$, where v_F^0 is the bare

Fermi velocity normal to the Fermi surface (this is obtained by approximating $\varepsilon_k \simeq v_F^0(k - k_F)$ in Eq. (22)). Lorentzian lineshapes were indeed observed for the MDCs (Fig. 9).

As an example of this kind of analysis we will briefly discuss the case of electron-phonon coupling on metallic surfaces, for which the established theoretical formalism can be applied very effectively [86,107–112]. The electron-phonon interaction involving surface phonons and the $\bar{\Gamma}$ -surface state on the Be(0001) surface was investigated by two groups, and qualitatively similar conclusion were drawn [107,108,110,111]. Figure 15(a) shows results for the Be(0001) surface state along the $\bar{\Gamma}\bar{M}$ direction of the surface Brillouin zone; a feature is seen dispersing towards the Fermi level [107]. Close to E_F the spectral function exhibits a complex structure characterized by a broad hump and a sharp peak, with the latter being confined to within an energy range given by the typical bandwidth ω_{ph} of the surface phonons. This behavior corresponds to a “two-branch” splitting of the near- E_F dispersion, with a transfer of spectral weight between the two branches as a function of binding energy. While the high-energy dispersion is representative of the bare quasiparticles, at low energy the dispersion is renormalized by the electron-phonon interaction (this behavior is shown, for a similar electron-phonon coupled system, in the inset of Fig. 15(b)). In other words, the weaker dispersion observed at energies smaller than ω_{ph} describes dressed quasiparticles with an effective mass enhanced by a factor of $(1 + \lambda)$, where λ is the electron-phonon coupling parameter [114]. The latter can also be estimated from the ratio of renormalized (v_k) and bare (v_k^0) quasiparticle velocities, according to the relation $v_k = \hbar^{-1} \partial \varepsilon_k / \partial k = (1 + \lambda)^{-1} v_k^0$. This way, for the data presented in Fig. 15(a) the value $\lambda = 1.18$ was obtained (alternatively λ can also be estimated from the temperature dependence of the linewidth near E_F [108]).

A similar example of electron-phonon coupled system is the surface of Mo(110) [113]. In this case, the real and imaginary part of the self energy shown in Fig. 15(b) were obtained directly from the EDC analysis: Σ'' corresponds to the EDC width and Σ' to the difference between the observed quasiparticle dispersion and a straight line approximating the dispersion of the non-interacting system (Fig. 15(b), inset). The step-like change at 30 meV in Σ'' is interpreted as the phonon contribution (dashed line) and the parabolic part at higher energies is attributed to electron-electron interactions. The phonon contribution to the real part of the self energy is calculated from the Kramers–Kronig relations (see Section 4) and agrees well with the data (dotted line). As an additional confirmation of the electron-phonon description, it was noted that the temperature dependence of the scattering rate is well reproduced by the calculations [113].

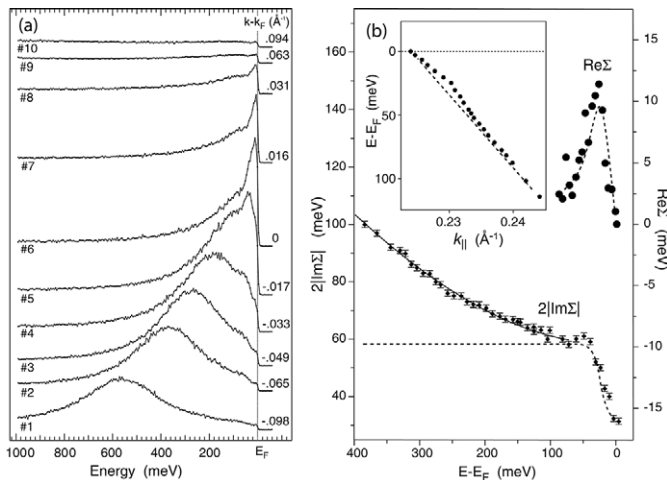


Fig. 15. (a) ARPES spectra for the Be(0001) surface state (from Ref. [107]). (b) Self energy estimated from the Mo(110) surface state ARPES spectra, and corresponding quasiparticle dispersion (inset). Calculated electron-phonon contributions to the real and imaginary part of $\Sigma(\mathbf{k}, \omega)$ are indicated by dotted and dashed lines, respectively (the latter was offset by 26 meV to account for impurity scattering). From Ref. [113].

Acknowledgments

Andrea Damascelli is grateful to B. Topi, M. Picchietto, and L. Nemo for their unlimited encouragement and cooperation. This work was supported by the Canada Research Chairs (CRC) Program and the Natural Science and Engineering Research Council of Canada (NSERC).

References

1. Hertz, H., *Ann. Phys.* **17**, 983 (1887).
2. Einstein, A., *Ann. Physik* **31**, 132 (1905).
3. Bachrach, R. Z., "Synchrotron Radiation Research, Advances in Surface and Interface Science," Vol. 1, (Plenum Press, New York, 1992).
4. Braun, J., *Rep. Prog. Phys.* **59**, 1267 (1996).
5. Brundle, C. R. and Baker, A. D., "Electron Spectroscopy: Theory, Techniques, and Applications," Vol. 1, (Academic Press, New York, 1977).
6. Brundle, C. R. and Baker, A. D., "Electron Spectroscopy: Theory, Techniques, and Applications," Vol. 2, (Academic Press, New York, 1978).
7. Cardona, M. and Ley, L., "Photoemission in Solids," Vol. 2, (Springer-Verlag, Berlin, 1978).
8. Carlson, T. A., "Photoelectron and Auger Spectroscopy," (Plenum Press, New York, 1975).
9. Courths, R. and Hüfner, S., *Phys. Rep.* **112**, 53 (1984).
10. Damascelli, A., Lu, D. H. and Shen, Z.-X., *J. Electron Spectr. Relat. Phenom.* **117–118**, 165 (2001).
11. Damascelli, A., Hussain, Z. and Shen, Z.-X., *Rev. Mod. Phys.* **75**, 473 (2003).
12. Eastman, D. E., in "Techniques of Metal Research," (edited by E. Passaglia), (Interscience Publisher, New York, 1972), Vol. VI, part I.
13. Feuerbacher, B. and Willis, R. F., *J. Phys. Solid State Phys.* **9**, 169 (1976).
14. Feuerbacher, B., Fitton, B. and Willis, R. F., "Photoemission on the Electronic Properties of Surfaces," (John Wiley & Sons, New York, 1978).
15. Grioni, M., *J. Electron Spectr. Relat. Phenom.* **117–118**, (2001), special issue on Strongly Correlated Systems.
16. Himpsel, F. J., *Adv. Phys.* **32**, 1 (1983).
17. Hüfner, S., "Photoelectron Spectroscopy," (Springer-Verlag, Berlin, 1995).
18. Inglesfield, J. E. and Holland, B. W., in "The Chemical Physics of Solid Surfaces and Heterogeneous Catalysis," (edited by D. A. King and D. P. Woodruff), (Elsevier Scientific Publishing Co., Amsterdam, 1981), Vol. 1.
19. Kevan, S. D., "Angle Resolved Photoemission-Theory and Current Applications," (Elsevier Science, Amsterdam, 1992).
20. Leckey, R. C. G., *Appl. Surf. Sci.* **13**, 125 (1982).
21. Ley, L. and Cardona, M., "Photoemission in Solids," Vol. II, (Springer-Verlag, Berlin, 1979).
22. Lindau, I. and Spicer, W. E., in "Synchrotron Radiation Research," (edited by H. Winick and S. Doniach), (Plenum Press, New York, 1980).
23. Lynch, D. W. and Olson, C. G., "Photoemission Studies of High-Temperature Superconductors," (Cambridge University Press, Cambridge, 1999).
24. Mahan, G. D., in "Electron and Ion Spectroscopy of Solids," (edited by L. Fiermans, J. Vennik, and W. Dekeyser), (Plenum Press, New York, 1978).
25. Margaritondo, G. and Weaver, J. H., in "Methods of Experimental Physics: Surfaces," (edited by M. G. Legally and R. L. Park), (Academic Press, New York, 1983).
26. Nemoshkalenko, V. V. and Aleshin, V. G., "Electron Spectroscopy of Crystals," (Plenum Press, New York, 1979).
27. Plummer, E. W. and Eberhardt, W., in "Advances in Chemical Physics," (edited by I. Prigogine and S. A. Rice), (John Wiley & Sons, New York, 1982), Vol. XLIV.
28. Shen, Z.-X. and Dessau, D. S., *Phys. Rep.* **253**, 1 (1995).
29. Smith, N. V., *Crit. Rev. Solid State Sci.* **2**, 45 (1971).
30. Smith, N. V. and Himpsel, F. J., in "Handbook on Synchrotron Radiation," (edited by E.-E. Koch), (North-Holland, Amsterdam, 1983), Vol. Ib.
31. Smith, K. E. and Kevan, S. D., *Prog. Solid State Chem.* **21**, 49 (1991).
32. Wendin, G., "Breakdown of the One-Electron Pictures in Photoelectron Spectroscopy," (Springer-Verlag, Berlin, 1981).
33. Wertheim, G., in "Electron and Ion Spectroscopy of Solids," (edited by L. Fiermans, J. Vennik, and W. Dekeyser), (Plenum Press, New York, 1978).
34. Williams, R. H., Srivastava, G. P. and McGovern, I. T., *Rep. Prog. Phys.* **43**, 1357 (1980).
35. Meinders, M. B. J., Ph.D. Thesis (1994). University of Groningen, The Netherlands.
36. Mahan, G. D., *Phys. Rev. B* **2**, 4334 (1970).
37. Pillo, T., Ph.D. Thesis (1999), University of Freiburg, Switzerland.
38. Strocov, V. N., Starnberg, H. I., Nilsson, P. O., Brauer, H. E. and Holleboom, L. J., *Phys. Rev. Lett.* **79**, 467 (1997).
39. Strocov, V. N. *et al.*, *Phys. Rev. Lett.* **81**, 4943 (1998).
40. Hansen, E. D., Miller, T. and Chiang, T.-C., *Phys. Rev. Lett.* **80**, 1766 (1998).
41. Smith, N. V., Thiry, P. and Petroff, Y., *Phys. Rev. B* **47**, 15476 (1993).
42. Miller, T., McMahon, W. E. and Chiang, T.-C., *Phys. Rev. Lett.* **77**, 1167 (1996).
43. Hansen, E. D., Miller, T. and Chiang, T.-C., *Phys. Rev. B* **55**, 1871 (1997).
44. Hansen, E. D., Miller, T. and Chiang, T.-C., *Phys. Rev. Lett.* **78**, 2807 (1997).
45. Mitchell, K., *Proc. Roy. Soc. London A* **146**, 442 (1934).
46. Makinson, R. E. B., *Phys. Rev.* **75**, 1908 (1949).
47. Buckingham, M. J., *Phys. Rev.* **80**, 704 (1950).
48. Schaich, W. L. and Ashcroft, N. W., *Phys. Rev. B* **3**, 2452 (1971).
49. Feibelman, P. J. and Eastman, D. E., *Phys. Rev. B* **10**, 4932 (1974).
50. Pendry, J. B., *Surf. Sci.* **57**, 679 (1976).
51. Pendry, J. B., *J. Phys. Solid State Phys.* **8**, 2413 (1975).
52. Liebsch, A., *Phys. Rev. B* **13**, 544 (1976).
53. Liebsch, A., in "Electron and Ion Spectroscopy of Solids," (edited by L. Fiermans, J. Vennik, and W. Dekeyser), (Plenum Press, New York, 1978).
54. Lindroos, M. and Bansil, A., *Phys. Rev. Lett.* **75**, 1182 (1995).
55. Lindroos, M. and Bansil, A., *Phys. Rev. Lett.* **77**, 2985 (1996).
56. Bansil, A. and Lindroos, M., *J. Phys. Chem. Solids* **56**, 1855 (1995).
57. Bansil, A. and Lindroos, M., *J. Phys. Chem. Solids* **59**, 1879 (1998).
58. Bansil A. and Lindroos, M., *Phys. Rev. Lett.* **83**, 5154 (1999).
59. Fan, H. Y., *Phys. Rev.* **68**, 43 (1945).
60. Berglund, C. N. and Spicer, W. E., *Phys. Rev.* **136**, A1030 (1964).
61. Sawatzky, G. A., *Nature* **342**, 480 (1989).
62. Gadzuk, J. W. and Šunjić, M. *Phys. Rev. B* **12**, 524 (1975).
63. Siegbahn, K. *et al.*, "ESCA Applied to Free Molecules," (North Holland, Amsterdam, 1969).
64. Abrikosov, A. A., Gor'kov, L. P. and Dzyaloshinskii, I. E., "Quantum Field Theoretical Methods in Statistical Physics," (Pergamon Press, Oxford, 1965).
65. Hedin, L. and Lundqvist, S., in "Solid State Physics: Advances in Research and Applications," (edited by H. Ehrenreich, F. Seitz, and D. Turnbull), (Academic, New York, 1969), Vol. 23.
66. Fetter, A. L. and Walecka, J. D., "Quantum Theory of Many-Particle Systems," (McGraw-Hill, New York, 1971).
67. Mahan, G. D., "Many-Particle Physics," (Plenum Press, New York, 1981).
68. Economou, E. N., "Green's Functions in Quantum Physics," Vol. 7 of Springer Series in Solid State Science (Springer-Verlag, Berlin, 1983).
69. Rickayzen, G., "Green's Functions and Condensed Matter in Techniques of Physics," Vol. 7 (Academic Press, London, 1991).
70. Norman, M. R., Ding, H., Fretwell, H., Randeria, M. and Campuzano, J. C., *Phys. Rev. B* **60**, 7585 (1999).
71. Landau, L. D., *Sov. Phys. JETP* **3**, 920 (1956).
72. Landau, L. D., *Sov. Phys. JETP* **5**, 101 (1957).
73. Landau, L. D., *Sov. Phys. JETP* **8**, 70 (1959).
74. Pines D. and Nozières, P. "The Theory of Quantum Liquids," Vol. 1 (Benjamin, New York, 1966).
75. Luttinger, J. M., *Phys. Rev.* **121**, 942 (1961).
76. Hodges, C., Smith, H. and Wilkins, J. W., *Phys. Rev. B* **4**, 302 (1971).
77. Yeh, J. J. and Lindau, I., *Atom. Data Nucl. Data Tabl.* **32**, 1 (1985).
78. Nozières, P., "Theory of Interacting Fermi Systems," (Benjamin, New York, 1964).
79. Shirley, D. A., *Phys. Rev. B* **5**, 4709 (1972).
80. Gobeli, G. W., Allen, F. G. and Kane, E. O., *Phys. Rev. Lett.* **12**, 94 (1964).
81. Dietz, E., Becker, H. and Gerhardt, U., *Phys. Rev. Lett.* **36**, 1397 (1976).

82. Hermanson, J., Solid State Commun. **22**, 9 (1977).
83. Eberhardt, W. and Himpfel, F. J., Phys. Rev. B **21**, 5572 (1980).
84. Cooper, J. W., Phys. Rev. **128**, 681 (1962).
85. Molodtsov, S. L. *et al.*, Phys. Rev. Lett. **85**, 4184 (2000).
86. Valla, T. *et al.*, Science **285**, 2110 (1999).
87. Seah, M. P. and Dench, W. A., Surf. Interface Anal. **1**, 2 (1979).
88. Sekiyama, A. *et al.*, Nature **403**, 396 (2000).
89. Mazin, I. I. and Singh, D. J., Phys. Rev. Lett. **79**, 733 (1997).
90. Damascelli, A. *et al.*, Phys. Rev. Lett. **85**, 5194 (2000).
91. Singh, D. J., Phys. Rev. B **52**, 1358 (1995).
92. Oguchi, T., Phys. Rev. B **51**, 1385 (1995).
93. Mackenzie, A. P. *et al.*, Phys. Rev. Lett. **76**, 3786 (1996).
94. Bergemann, C., Julian, S. R., Mackenzie, A. P., NishiZaki, S. and Maeno, Y., Phys. Rev. Lett. **84**, 2662 (2000).
95. Yokoya, T. *et al.*, Phys. Rev. B **54**, 13311 (1996).
96. Yokoya, T. *et al.*, Phys. Rev. Lett. **76**, 3009 (1996).
97. Lu, D. H. *et al.*, Phys. Rev. Lett. **76**, 4845 (1996).
98. Puchkov, A. V., Shen, Z.-X., Kimura, T. and Tokura, Y., Phys. Rev. B **58**, 13322 (1998).
99. Matzdorf, R. *et al.*, Science **289**, 746 (2000).
100. Damascelli, A. *et al.*, J. Electron Spectr. Relat. Phenom. **114–116**, 641 (2001).
101. Damascelli, A., Shen, K. M., Lu, D. H. and Shen, Z.-X., Phys. Rev. Lett. **87**, 239702 (2001).
102. Shen, K. M. *et al.*, Phys. Rev. B **64**, 180502 (2001).
103. Corcoran, R. *et al.*, J. Phys. Cond. Matt. **6**, 4479 (1994).
104. Straub, T. *et al.*, Phys. Rev. Lett. **82**, 4504 (1999).
105. Damascelli, A., (2000), unpublished.
106. Yokoya, T. *et al.*, Science **294**, 2518 (2001).
107. Hengsberger, M., Purdie, D., Segovia, P., Garnier, M. and Baer, Y., Phys. Rev. Lett. **83**, 592 (1999).
108. Balasubramanian, T., Jensen, E., Wu, X. L. and Hulbert, S. L., Phys. Rev. B **57**, 6866 (1998).
109. Hofmann, P., Cai, Y. Q., Grüter, C. and Bilgram, J. H., Phys. Rev. Lett. **81**, 1670 (1998).
110. Hengsberger, M., Fresard, R., Purdie, D., Segovia, P., and Baer, Y., Phys. Rev. B **60**, 10796 (1999).
111. LaShell, S., Jensen, E. and Balasubramanian, T., Phys. Rev. B **61**, 2371 (2000).
112. Rotenberg, E., Schaefer, J. and Keven, S. D., Phys. Rev. Lett. **84**, 2925 (2000).
113. Valla, T., Fedorov, A. V., Johnson, P. D. and Hulbert, S. L., Phys. Rev. Lett. **83**, 2085 (1999).
114. Ashcroft, N. W. and Mermin, N. D., “Solid State Physics,” (Saunders College, Philadelphia, 1976).